Making foam-like bioactive glass scaffolds by vat photopolymerization

Open Ceramics 15 (2023) 100392

Contents lists available at ScienceDirect

Open Ceramics

journal homepage: www.sciencedirect.com/journal/open-ceramics

# Making foam-like bioactive glass scaffolds by vat photopolymerization

Francesco Baino [a,*], Joana Dias [b], Mojtaba Alidoost [a,c], Martin Schwentenwein [b], Enrica Verné [a]

[a] Institute of Materials Physics and Engineering, Department of Applied Science and Technology (DISAT), Politecnico di Torino, Corso Duca Degli Abruzzi 24, 10129, Turin, Italy
[b] Lithoz GmbH, Mollardgasse 85a/2/64-69, 1060, Vienna, Austria
[c] J-Tech Interdepartmental Research Centre, Politecnico di Torino, Corso Duca Degli Abruzzi 24, 10129, Turin, Italy

ARTICLE INFO

Handling Editor: Dr P Colombo

*Keywords:*
Bioactive glass
Additive manufacturing
Stereolithography
Scaffold
Biomaterials

ABSTRACT

This study explores the feasibility of bioactive glass scaffolds by using a stereolithographic technology (digital light processing-based vat photopolymerization) as fabrication method and the micro-tomographic reconstruction of an open-cell polymeric sponge as input virtual model to the printing system, in the attempt to replicate the trabecular architecture of cancellous bone. Additively-manufactured scaffolds were investigated from morphological (scanning electron microscopy), microstructural (X-ray diffraction), mechanical (compressive tests) and bioactive viewpoints (immersion studies in simulated body fluid (SBF)). Well-densified foam-like glass scaffolds were obtained after sintering, provided with suitable mechanical properties (compressive strength 21.9 ± 6.2 MPa, elastic modulus 4.8 ± 0.1 GPa, Weibull modulus 3.9) for bone-contact applications. The formation of a hydroxyapatite layer on scaffold struts after soaking in SBF also demonstrated the in vitro bioactivity of the printed structures.

## 1. Introduction

Scaffolds for bone tissue engineering are porous structures acting as biocompatible templates that, after being implanted in vivo, promote the regeneration of newly-formed, healthy osseous tissue at the defective site, thus accelerating bone healing [1].

An ideal scaffold for bone repair should exhibit an architectural similarity with cancellous bone, including a trabecular-like interconnected macroporosity to allow biological fluid perfusion, cell colonization, and new blood vessel development/ingrowth [2,3]. Furthermore, the scaffold should not release toxic by-products upon contact with the body environment, be osteoconductive (i.e., promoting osteoblast attachment onto its surface) and osteoinductive (i.e., stimulating bone cell activity and osteogenesis at the genetic level), and be mechanically suitable to interact with the host bone and support new bone [4].

Indeed, the properties of a scaffold are dictated by both the biomaterial used for its fabrication and the method selected to obtain the porous structure. After being invented in 1969 by Larry Hench [5], bioactive glasses have been introduced 30 years ago in the clinical practice and, since then, millions of patients worldwide have benefitted from their implantation [6]. They are used especially in orthopaedics and dentistry in the form of particles, injectable pastes, coatings and porous scaffolds able to bond to bone creating a stable interface with living tissue and promote bone healing by stimulating osteogenesis and angiogenesis in situ [7].

Conventional methods to fabricate porous bioactive glass scaffolds mainly rely on (i) foaming methods, (ii) blending glass powders with pore-forming agents (e.g. polymeric or soluble particles) or (iii) using a sacrificial template (porous polymer), followed by burning-off of the organic matter and sintering of the glass [8]. These fabrication methods, however, typically suffer from difficult scalability for mass production and the quality of the final product is often operator-dependent.

The implementation of additive manufacturing technologies in the field of biomedical scaffolds over the last two decades has allowed achieving significant improvements in the fine-tuning of pore shape, size and spatial arrangement as well as in the reproducibility of implants architecture [9]. This was possible due to the introduction of computer-aided design (CAD) and computer-aided manufacturing (CAM) technologies in the processing flowchart of biomaterials, including bioactive ceramics [10]. The potential, existing limitations and challenges of additive manufacturing approaches applied to bioactive glasses have been recently reviewed [11].

At present, digital light processing vat photopolymerization (DLP-

* Corresponding author.
*E-mail address:* francesco.baino@polito.it (F. Baino).

https://doi.org/10.1016/j.oceram.2023.100392
Received 20 March 2023; Received in revised form 17 June 2023; Accepted 19 June 2023
Available online 19 June 2023

VPP), belonging to the class of stereolithographic methods, allows achieving the best spatial resolution among the additive manufacturing technologies used for the processing of ceramic materials (around 35–40 μm in commercial systems [12] and up to 1.2 μm if micro-lithographic apparatus is used [13]). DLP-VPP relies on using a dynamic mask to promote the single-step layerwise polymerization of a photocurable resin embedding ceramic particles inside. Compared to other additive manufacturing technologies, this bottom-up method is faster, yields fewer defects in the printed product, and avoid using too much excess material during the printing process [14]. Tesavibul et al. [15] first reported in 2012 the application of DLP-VPP to fabricate 45S5 Bioglass® scaffolds with grid structure. Other additive manufacturing technologies were then proposed, such as robocasting [16,17] which does not require too expensive equipment like DLP-VPP.

Despite economic affordability, extrusion-based additive manufacturing methods suffer from the limitation of having ceramic or glass filaments as "structural units" of the scaffold, leading to assembling 3D grids of material intercalated by parallel or strongly-oriented channels, which does not closely replicate the trabecular architecture of bone. In this regard, conventional methods like foam replication are more effective to produce truly bone-like scaffolds [18]. In order to take the best from the two approaches, DLP-VPP and sponge replication have been recently "merged" for producing hydroxyapatite scaffolds using a micro-tomographic reconstruction of a polyurethane foam as the input (virtual model) to the printing system [19,20]. The present work aims at exploring the feasibility of this approach to fabricate DLP-printed bioactive glass scaffolds with structure and mechanical properties as close as possible to cancellous bone. To the best of the authors' knowledge, this is the first study in which "non-grid" ("non-rectilinear") porous scaffolds are produced by processing a bioactive glass through DLP-VPP and further expands the potential of this technology with respect to the seminal research work reported in Ref. [15].

## 2. Materials and methods

### 2.1. Glass and slurry preparation

The silicate glass selected for scaffold manufacturing, coded as 47.5 B (composition 47.5$SiO_2$–10$Na_2O$–10$K_2O$–10MgO–20CaO-2.5$P_2O_5$ mol. %), was produced using a melt-quenching method in standard conditions. The high-purity reagents (oxides and carbonates), all purchased from Sigma-Aldrich/Merck, were homogenously mixed in plastic bottles onto rotating rollers overnight to promote the homogeneity of the mix and were then put inside a platinum crucible at room temperature. The powder mix was hand-pressed to reduce the air inside the blend to minimum and the crucible was then put inside an electrically-heated furnace (Nabertherm GmbH, Germany) to reach melting at 1500 °C.

The melt was then quenched in cold water at room temperature to produce the "frit", which was dried and ball milled in a planetary milling machine with six zirconia spheres (Pulverisette 6, Fritsch, Germany). Particles were sifted below 32 μm using a stainless steel sieve (Giuliani Technologies Srl, Torino, Italy) because, according to previous experience, this particle size is suitable to produce 47.5 B glass-derived porous scaffolds for bone replacement by other technologies like robocasting and foam replication [21,22].

Glass powders were dried for about 24 h at 120 °C and added in 3 steps to a previously prepared organic batch containing low viscous solvent, reactive monomers based on acrylate and methacrylate chemistry, and photoinitiator (less than 1 wt%). This sequential addition of glass powders was necessary to ensure easy mixing and homogeneity of the slurry. Mixing at each stage (1800 rpm for 30 s followed by 2750 rpm for 30 s) was performed by using a SpeedMixerTM DAC 400.1 FVZ (Hauschild, Germany) working as dual asymmetric centrifuge consisting of a mixing arm and a mixing cup, rotating in opposite directions. Once all the powders were added to the binder, the slurry underwent a dispersion process with milling beads for 3 h prior to being finally stored at 5 °C, ready for use.

### 2.2. Printing procedure

VPP of 47.5 B-derived scaffolds was performed by using a CeraFab 7500 3D printer including CeraFab control data pre-processing software. The virtual model of the scaffold was acquired and used as a 3D CAD file in stl format.

For this study, a CAD file deriving from the micro-tomographic reconstruction of a 45-ppi commercial polyurethane sponge was used as scaffold model, following the approach reported in a previous work [19]. Image elaboration through InVesalius software allowed recreating the 3D profile of original sponge cuboids and then modifying the virtual object in order to obtain a cylindrical shape with an aspect ratio of 2:1 (diameter 5 mm, height 10 mm). Shrinkage compensation factors (1.258 along x/y axes and 1.437 along z axis) were calculated on preliminary printing trials on non-porous specimens and, hence, the CAD model was properly scaled to yield sintered scaffolds with dimensions close to the nominal ones. A contour offset was also added to the. stl file and the thickness of the solid skeleton (struts) was increased by 40% in order to ensure successful printability and mechanical integrity of final scaffolds.

The used DLP system included powerful LEDs as a light source in the blue visible region and a digital mirror device (DMD) chip as a dynamic mask with a resolution of 1920 × 1080 pixels and a pixel size of 40 × 40 μm [23]. The DMD chip of CeraFab 7500 guaranteed a selective photopolymerization of the layer; the resolution in the x-y plane was 40 μm, the thickness of a single layer was set at 25 μm and the DLP energy was adjusted to 400 mJ/$cm^2$. Layer-by-layer production involves the addition of fresh slurry once a layer is produced. The printing process started with a complete rotation of the vat, then the building platform moved towards the vat until a gap equal to the height of a single layer was achieved. The next step involved the selective exposure of the slurry by visible blue light with consequent polymerization of the desired area. In order to facilitate the separation between the newly-formed layer and the surface of the vat, the latter was slowly tilted downwards and the building platform was simultaneously raised to finalize the fabrication of an individual layer. The sequence of this process was then repeated for the remaining layers until the entire printing job was completed.

After being removed from the building platform, the printed green samples were carefully cleaned to eliminate the uncured slurry with compressed air and the cleaning medium LithaSol.

The thermal post-processing protocol was designed according to previous experience with ceramic slurries based on a similar organic binder system. Specifically, a multistage thermal treatment in air was applied to printed greens, including a debinding step at 430 °C for 6 h followed by a sintering phase at 650 °C for 1 h. This sintering temperature was selected to obtain glassy scaffolds and avoid crystallization, which was reported to begin around 700 °C for the 47.5 B compositional system [22].

### 2.3. Characterizations

#### 2.3.1. Microstructure

47.5 B-derived scaffolds were pulverized by ball milling and the resulting powder was analysed by wide-angle (2θ range: 10–60°) X-ray diffraction (XRD; X'Pert Pro PW3040/60 diffractometer with Bragg-Brentano camera geometry, PANalytical, Eindhoven, The Netherlands). Cu Kα incident radiation was used (wavelength λ = 0.15405 nm); operating parameters included 40 kV voltage, 30 mA filament current, 0.02° angular step size and 1 s fixed counting time per step. The analysis of XRD pattern was performed through X'Pert HighScore software (2.2 b) equipped with the PCPDFWIN database for the identification of crystalline phases. XRD on the starting 47.5 B powder was also performed for comparative purpose, using the same experimental conditions mentioned above.

#### 2.3.2. Morphology and porosity

The surface characteristics and overall porous architecture of sintered scaffolds were investigated by filed-emission scanning electron microscopy (FE-SEM; SupraTM 40, Zeiss, Oberkochen, Germany) at an accelerating voltage of 5 kV.

The total porosity (%) of the scaffolds was assessed by mass-volume measurements as $p = (1 - \rho/\rho_0) \times 100$, where ρ is the bulk (apparent) density of the scaffold and $\rho_0$ is the theoretical density of non-porous materials which was assessed through the Archimedes method (2.64 g/cm$^3$ [24]).

The volumetric shrinkage (%) of scaffolds was also estimated as $(1 - V/V_0) \times 100$, where V is the volume of sintered scaffold and $V_0$ is the volume of non-sintered green body.

Porosity and volumetric shrinkage were expressed as average ± standard deviation on 22 samples (the same used for mechanical characterization, see section 2.3.3).

#### 2.3.3. Mechanical properties

Scaffolds underwent uniaxial compression perpendicularly to the bases of the porous cylinder. The compressive strength (σ) was calculated as the ratio $\frac{L}{A}$, where L is the peak load recorded during the test and A is the initial contact surface (i.e., the resistant cross-sectional area). This test was performed on 22 samples by using the MTS Criterion Model 43 machine (cell load 44 kN) imposing a cross-head speed of 0.5 mm/min. Samples were polished before being tested in order to obtain a perfect parallelism between the two bases.

The elastic modulus was determined from the initial linear region of the stress strain curve.

The fracture energy per unit volume (W), which Eq. (1) defines as the energy needed to deform the sample from the unloaded condition to the failure strain $\epsilon_f$ (corresponding to the peak stress), was calculated by the analysis of the area under the stress-strain curve until the failure point is reached:

$$W = \int_0^{\varepsilon_f} \sigma(\varepsilon) d\varepsilon \quad (1)$$

Compressive strength, elastic modulus and fracture energy were expressed as average ± standard deviation.

The Weibull modulus *m* of the scaffolds, which is measure of material reliability, was determined according to the procedure described in the ASTM C1239-07 [25], which also recommends at least 20 specimens to be tested. The parameter *m* can be assessed by least-square fitting of Eq. (2), containing data from compressive tests:

$$\ln\left(\ln\left(\frac{1}{1-P_f}\right)\right) = m\ln(\sigma) - m\ln(\sigma_0) \quad (2)$$

where $P_f$ was the probability of failure at a stress σ and $\sigma_0$ was the Weibull scale parameter.

Hence, a plot of $\ln\left(\ln\left(\frac{1}{1-P_f}\right)\right)$ vs. $\ln(\sigma)$ followed by linear regression gives a straight line of slope *m*. The failure stresses must be ordered in ascending order and the failure probability $P_f$ is estimated as $(i - 0.5)/N$, where $N = 22$ is the total number of scaffolds tested and $i = 1, 2, \ldots N$ is the specimen rank.

#### 2.3.4. In vitro bioactivity

The apatite-forming ability of scaffolds was assessed by standard in vitro bioactivity studies through immersion in Kokubo's simulated body fluid (SBF) [26]. Triplicate tests were carried out for five different periods of time (24 h, 48 h, 7 days, 15 days and 1 month) under dynamic controlled conditions inside an orbital shaker (rotational velocity 100 rpm, temperature 37 °C) without any refresh of the solution. Mass-to-liquid ratio was fixed to 1.5 mg/mL, as commonly adopted for in vitro bioactivity studies in SBF when specimens with high surface area are tested, including powders and porous scaffolds [27]. The solution pH was recorded at each timepoint (end of experiments).

Morphological analyses by SEM (equipped with energy-dispersive spectroscopy (EDS) for compositional analysis) were performed on SBF-treated scaffolds using experimental conditions analogous to those described in section 2.3.2.

SBF-treated scaffolds were non-destructively analysed by micro-computed tomography (micro-CT) to highlight the surface-reaction layer. A customized equipment available at the Interdepartmental Centre "J-Tech" at Politecnico di Torino and installed by the Fraunhofer-Institut für Keramische Technologien und Systeme (IKTS, Dresden, Germany) was used for this purpose. Projection images were collected using a source voltage of 50 kV and a source current of 180 μA, along with a source-to-object distance of 58 mm and a source-to-detector distance of 1500 mm. No filter was used and the voxel size was 9.3 μm. Rotation step size was 0.225°, exposure time was 1 s per projection. ImageJ software allowed visualizing the 3D reconstructed volumes of scaffolds.

XRD was also performed on intact SBF-treated scaffolds following the same experimental setup already described in section 2.3.1.

## 3. Results and discussion

The VPP experiments using a foam-like model as the input CAD file to the printing system led to the successful fabrication of replicas of the virtual template. Despite their highly-porous structure, the green samples could be manipulated after printing without undergoing any apparent damage (Fig. 1a); the orange colour was due to the presence of the organic phase that will be removed during thermal debinding. The cleaning process, too, did not involve any damage to the printed parts that could be eventually sintered to obtain the 47.5 B-derived scaffolds (Fig. 1b).

Fig. 1c shows that the 3D pore-strut architecture of the scaffolds closely reproduces the foam-like structure of the open-cell polymeric template used as a printing model and, hence, the trabecular organization of cancellous bone. Sintering was effective, yielding well-densified struts (diameter in the range of 100–150 μm) with smooth surfaces where the original glass particles could not be detected anymore (Fig. 1d).

The total porosity was 34.5 ± 5.6 vol%, which is lower than the typical range of healthy human cancellous bone (from 50 vol% of femur neck to 85 vol% of iliac crest and vertebrae [28,29]). This issue will indeed require further optimization in the future to try approaching the optimal porosity range for bone tissue engineering scaffolds (above 50 vol% [30]); for example, reducing the thickness increase in the CAD model (contouring phase) as well as modulating the sintering temperature could be two approaches deserving future investigation. Printing fidelity will deserve to be studied as well; in this regard, prediction of the actual post-sintering volumetric shrinkage could be challenging, as some differences in the densification/sintering behaviour of foam-replicated glass scaffolds vs. non-porous glass products were observed in previous studies [31]. On the other hand, a scaffold volumetric shrinkage of 58.6 ± 5.9% was assessed in the present work, which is line with the early measurements on non-porous glass beams (56%) that were carried out to determine the shrinkage compensation factors.

Fig. 2 shows the XRD patterns obtained from the analysis of as-such 47.5 B powder and powdered scaffold after sintering. Before being thermally treated at high temperature, the material is amorphous as revealed by the broad halo in the 2θ-range within 25–35°, which is typical of silicate glasses. After the sintering process at 650 °C for 1 h, some low-intensity diffraction peaks were detected suggesting the partial devitrification of the glass associated to the development of one crystalline phase suggesting the formation of crystalline phases ($Ca_2SiO_4$, reference code 00-020-0236). However, the material is predominantly amorphous, as confirmed by the broad diffraction halo that is still well visible in Fig. 2a. According to sinter-crystallization studies

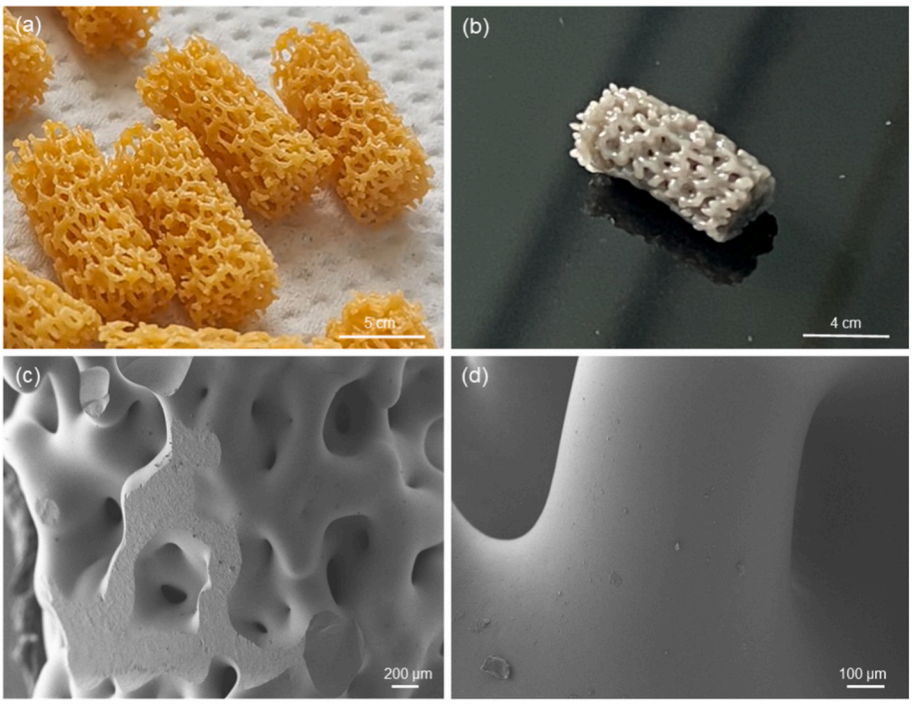


**Fig. 1.** Results of the printing process: (a) cleaned greens; (b) sintered scaffolds; (c) and (d) SEM micrographs showing the porous architecture of final scaffolds at different magnifications ((c) 80×, (d) 500 X).

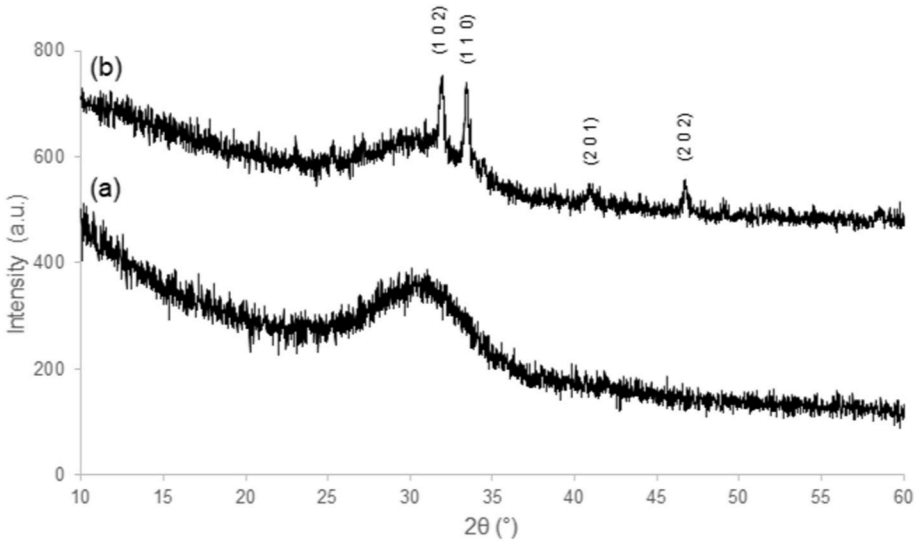


**Fig. 2.** XRD patterns of (a) initial 47.5 B powder and (b) pulverized scaffold (after sintering at 650 °C); the marked peaks correspond to $Ca_2SiO_4$.

on the same 47.5 B glass reported in a previous publication [24], this calcium silicate is expected to evolve into a combeite-type phase ($Na_2Ca_2(Si_3O_9)$) at higher temperature that was also found in sintered 45S5 Bioglass® [32,33], which is the reference material for bioactive glasses and glass-ceramics in terms of biocompatibility and bioactivity. In this regard, other authors showed that the presence of calcium silicate phases in crystallized 45S5 Bioglass® can decrease the bioactivity, without totally suppressing it [34]; the apatite-forming ability in vitro was also preserved in the DLP-processed scaffolds analysed in the present study, as revealed by immersion studies in SBF (reported later).

The compressive strength of scaffolds was 21.9 ± 6.2 MPa, which is a little bit higher than the standard reference for human trabecular bone (2–12 MPa [35]) and may suggest application also in load-bearing sites. Fig. 3 displays an example of stress-strain curve obtained from the compression test: the multi-step profile, which is typical of brittle cellular materials like porous bioactive glasses [32], reflects the sequential fracture of the scaffold struts during the compression since every fracture event generates a step in the curve. The curve starts with a positive slope until the first peak, which corresponds to the first cracking event. This yields a decrease of the stress (negative slope) but the material is still able to withstand the applied load and, thus, the stress can increase again with another positive slope. The repetition of this behaviour results in the formation of a sawtooth profile, typical for foam-like ceramics [36].

The elastic modulus of scaffolds was 4.8 ± 0.1 GPa, which is significantly higher than that of cancellous bone (0.05–0.5 GPa) and even reflects the order magnitude for human cortical bone (7–30 GPa [37]). This suggests, in combination with the remarkable values of

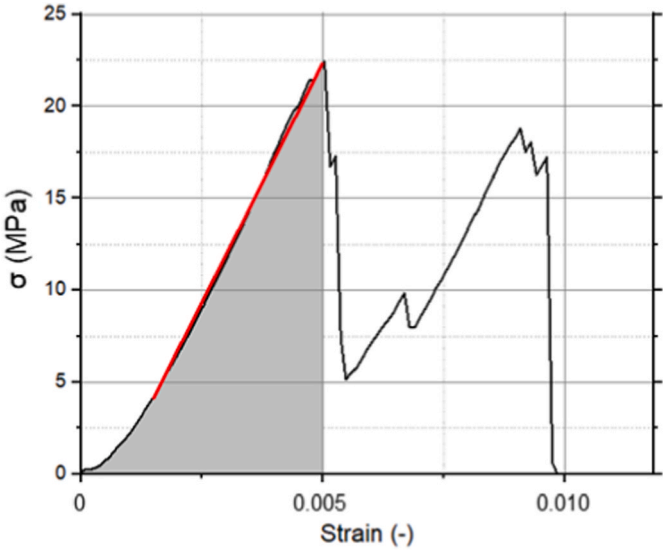


**Fig. 3.** Representative stress-strain curve obtained during compressive tests on sintered scaffold.

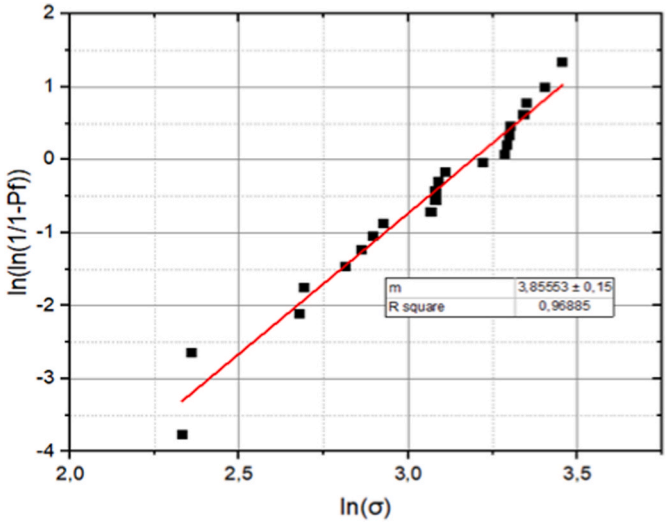


**Fig. 4.** Weibull plot with linear fitting for 47.5 B glass-derived scaffolds.

compressive strength, the possible application of such scaffolds for the repair of high-load-bearing defect sites.

The fracture energy was calculated to be 71.1 ± 33.5 kJ/m$^3$; this mechanical parameter is seldom reported in the literature for glass-derived scaffolds, which makes a comparison really difficult to be carried out. In general, porous glass or ceramic scaffolds are expected to show a limited energy absorption capacity until failure. A comparable fracture energy value of 93 kJ/m$^3$ was assessed for 47.5 B-derived scaffolds produced by robocasting (same material composition used in the present study but different additive manufacturing method) [38]. Looking at other glass systems, foam-like phosphate glass scaffolds exhibited a value of fracture energy of 20 kJ/m$^3$ [39], which could be increased up to 150 kJ/m$^3$ by processing the same glass through polyethylene burn-off method that, however, yielded lower porosity, pore size and interconnectivity [40].

The Weibull modulus ($m$) determined from the strength data for a relatively large number of identical samples (typically more than 20) is commonly used as a measure of the probability of failure of brittle materials under a given stress. The mechanical response of brittle materials – including glass scaffolds – is sensitive to microstructural flaws such as pores and microcracks. In this study, a value of $m$ = 3.9 was obtained along with the related Weibull scale parameter $\sigma_0$ = 23.4 MPa, which was determined by knowing the intercept of the linear fit (−12.3) reported in Fig. 4. Comparison with previous results from the literature is interesting; for example, the same 47.5 B glass was printed by robocasting to produce grid-like scaffolds, yielding a Weibull modulus of 3.1 [38]. There are relatively few studies in the literature reporting the Weibull modulus for scaffolds based on other bioceramics or glass compositions by additive manufacturing technologies. Martinez-Vazquez et al. [41] increased the Weibull modulus of robocast phosphate scaffolds from 3.0 to more than 7.5 by polymer infiltration. The same strategy was reported by Eqtesadi et al. [42] in the case of robocast 13–93 scaffolds, revealing an analogous percentage improvement in terms of Weibull modulus after polymer infiltration (from 8.0 to 15.0). Higher values of the Weibull modulus in non-polymer-coated bioceramics were obtained under compression for 3D-printed scaffolds with an oriented microstructure along the direction of anisotropy ($m$ up to 9) [43]. A comparison with some mechanical results from the literature is summarized in Table 1.

During in vitro bioactivity studies, the pH of SBF was checked once the tests ended for every sample solution and a rapid increase was observed in the first 24 h, followed by a stabilization over the residual period of immersion (plateau value of 7.71 ± 0.01). These pH values are beneficial for bone regeneration as a moderate alkaline environment (<9) stimulates osteoblast viability and, hence, promotes osteogenesis [44].

XRD performed on intact scaffolds after immersion in SBF revealed the formation of hydroxyapatite (reference code: 00-001-1008) on the surface of scaffold struts, as demonstrated by the presence of two small peaks at 2θ = 26° and 32° which could be referred to the (0 0 2) and (2 1 1) reflections, respectively (Fig. 5).

Fig. 6 shows the evolution of scaffold surface during the soaking period in SBF. In good agreement with the bioactivity mechanism proposed by Hench for silicate bioactive glasses [45], the presence of a surface silica gel layer is already visible at 1 day after immersion; this layer grew in thickness over time eventually evolving in a hydroxyapatite "skin" lining the scaffold struts. Cracking of this surface layer is due to the drying of the scaffold and the high vacuum applied in the chamber of SEM equipment.

SEM inspection at high magnification (Fig. 7) shows the formation of calcium phosphate nuclei on the top of silica gel after 1 day, followed by the progressive formation of globular agglomerates assuming a "cauliflower" morphology, which is typical of bone-like apatite. The nanocrystalline nature of newly-formed hydroxyapatite can be well appreciated in Fig. 7d.

The Ca/P atomic ratio assessed by EDS analysis stabilized around 1.4 after 1 month of immersion in SBF, revealing the Ca-deficient nature of the hydroxyapatite formed on scaffold struts (Ca/P value of stoichiometric hydroxyapatite = 1.67). This is consistent with the results reported in previous studies about in vitro bioactivity of bioactive glasses, showing the typical formation of Ca-deficient hydroxyapatite on the material surface [21,24,46].

The evolution of the surface reaction layer over time upon immersion in SBF was also visualized by micro-CT imaging: qualitative analysis of scaffold cross-sections (Fig. 8) allowed clearly discriminating the scaffold material (light grey), the intermediate silica gel (dark grey) and the top hydroxyapatite layer (light grey) according to a material-density basis (the darker the colour, the lower the material density; void spaces (i.e., pores filled by air) correspond to black [47]). These findings are consistent with analogous results reported for SBF-treated grid-like 47.5 B glass scaffolds produced by robocasting [21]. It is worth pointing out that the reaction layer can be observed not only on the outer surface of the scaffold but also on the walls of the inner pores (see the red circles in Fig. 8), which are therefore interconnected and potentially able to allow biofluid perfusion and cell/new tissue ingrowth in vivo.

**Table 1**
Comparison of the mechanical properties of VPP-derived 47.B-based scaffolds produced in this work with other biomaterials and bone.

| Material | Compressive strength (MPa) | Elastic modulus (GPa) | Fracture energy (kJ/m$^3$) | Weibull modulus | References |
|---|---|---|---|---|---|
| 47.5 B glass scaffolds (foam, VPP) | 21.9 ± 6.2 | 4.8 ± 0.1 | 71.1 ± 33.5 | 3.9 | This work |
| 47.5 B glass scaffolds (grid, robocasting) | 6.1 ± 2.6 | 343 ± 145 | 93 ± 59 | 3.1 | [38] |
| 45S5 Bioglass® scaffolds (foam replication) | 0.27-0-42 | – | – | – | [32] |
| Phosphate glass scaffolds (polyethylene bur-off) | 1.5 ± 0.5 | – | 150 | – | [40] |
| Hydroxyapatite scaffolds (foam, VPP) | 1.60 ± 0.79 | 513 ± 290 | – | 2.2 | [19] |
| Trabecular bone | 2–12 | 0.05–0.5 | – | – | [35,37] |
| Cortical bone | 50–150 | 7–25 | – | – | [35,37] |

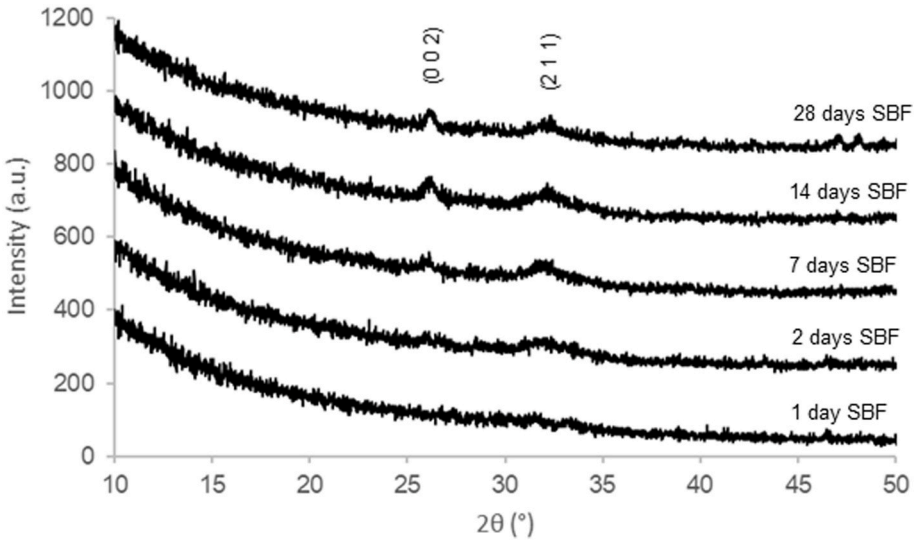


**Fig. 5.** XRD patterns of scaffolds after immersion in SBF for different time frames; the marked peaks correspond to newly-formed hydroxyapatite.

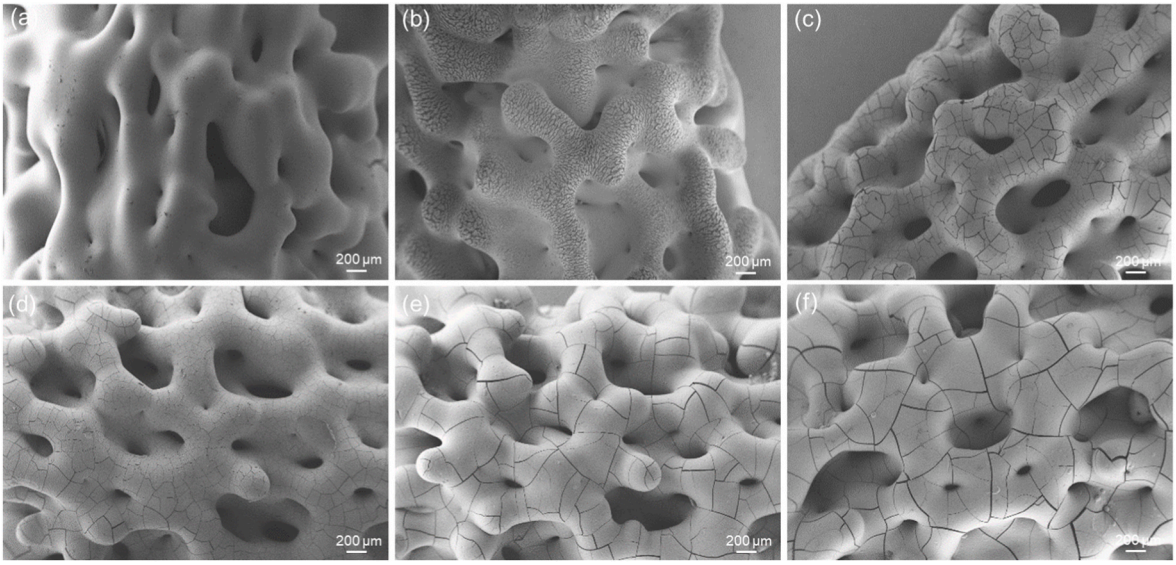


**Fig. 6.** SEM micrographs (magnification 80×) showing the gross evolution of scaffold surface during immersion in SBF: (a) 0 days (as-such sample), (b) 1 day, (c) 2 days, (d) 7 days, (e) 14 days and (f) 28 days.

## 4. Conclusions

This study has shown, for the first time, that bioactive glass scaffolds can be additively manufactured by VPP using a polymeric foam model from tomographic imaging as input CAD file to the printing system. As a result, it was possible to fabricate silicate bioactive glass scaffolds with 3D porous architecture mimicking that of cancellous bone as well as compressive strength and elastic modulus suitable for osseous applications. The glass scaffolds also exhibited bioactive properties in vitro, being coated by a layer of nanocrystalline hydroxyapatite upon immersion in SBF. This novel approach expands the potential of additive manufacturing to process biomaterials and, especially, bioactive glasses and ceramics, overcoming the limitations of printing grid structures and taking a step forward in the development of truly "bone-like"

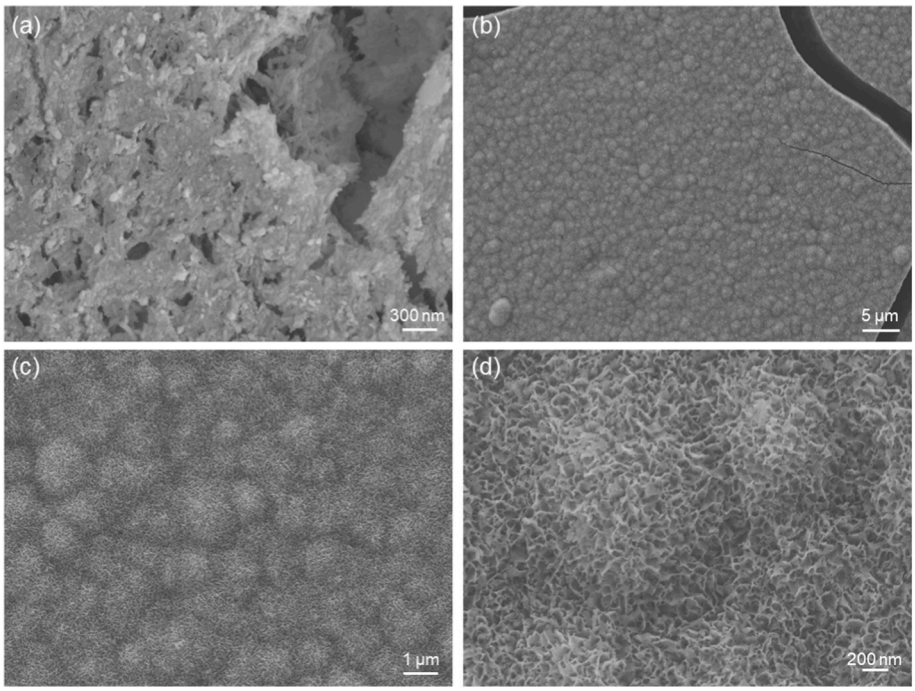


**Fig. 7.** SEM micrographs showing high-magnification details of scaffold surface during immersion in SBF: (a) newly-formed precipitates on the top of cracked silica at 1 day; (b) globular agglomerates of the new phase (hydroxyapatite) at 7 days, revealing a cauliflower morphology (c) with nanocrystalline nature (d). Magnifications: (a) 75,000×, (b) 5000 X, (c) 20,000 X, (d) 75,000 X.

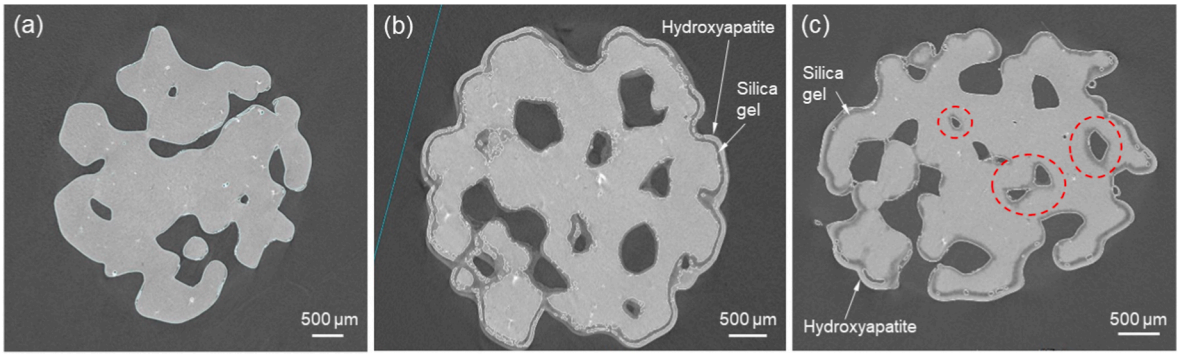


**Fig. 8.** Representative cross-sections from micro-CT analysis of (a) as-such scaffold, (b) scaffold soaked for 14 days in SBF, and (c) scaffolds soaked for 28 days in SBF. Red circles emphasize the reaction layers in internal pores. (For interpretation of the references to colour in this figure legend, the reader is referred to the Web version of this article.)

implantable devices for bone tissue engineering. The use of VPP technology to develop high-strength functionally-graded scaffolds mimicking the pore transition between cancellous and cortical bone and/or provided with other pore-strut 3D structures is under investigation and will be the topic of a future publication.

## Declaration of competing interest

The authors declare that they have no known competing financial interests or personal relationships that could have appeared to influence the work reported in this paper.

## References

[1] G. Hulsart Billström, A.W. Blom, S. Larsson, A.D. Beswick, Application of scaffolds for bone regeneration strategies: current trends and future directions, Injury 44 (2013) S28–S33.
[2] D.W. Hutmacher, Scaffolds in tissue engineering bone and cartilage, Biomaterials 21 (2000) 2529–2543.
[3] A.A. El-Rashidy, J.A. Roether, L. Harhaus, U. Kneser, A.R. Boccaccini, Regenerating bone with bioactive glass scaffolds: a review of in vivo studies in bone defect models, Acta Biomater. 62 (2017) 1–28.
[4] K.A. Hing, Bioceramic bone graft substitutes: influence of porosity and chemistry, Int. J. Appl. Ceram. Technol. 2 (2005) 184–199.
[5] L.L. Hench, The story of bioglass, J. Mater. Sci. Mater. Med. 17 (2006) 967–978.
[6] J.R. Jones, D.S. Brauer, L. Hupa, D.C. Greenspan, Bioglass and bioactive glasses and their impact on healthcare, Int. J. Appl. Glass Sci. 7 (2016) 423–434.
[7] F. Baino, Bioactive glasses - when glass science and technology meet regenerative medicine, Ceram. Int. 44 (2018) 14953–14966.
[8] F. Baino, E. Fiume, J. Barberi, S. Kargozar, J. Marchi, J. Massera, E. Verné, Processing methods for making porous bioactive glass-based scaffolds – a state-of-the-art review, Int. J. Appl. Ceram. Technol. 16 (2019) 1762–1796.
[9] D.W. Hutmacher, M. Sittinger, M.V. Risbud, Scaffold-based tissue engineering: rationale for computer-aided design and solid free-form fabrication systems, Trends Biotechnol. 22 (2004) 354–362.
[10] R. Gmeiner, U. Deisinger, J. Schönherr, B. Lechner, R. Detsch, A.R. Boccaccini, J. Stampfl, Additive manufacturing of bioactive glasses and silicate bioceramics, J. Ceram. Sci. Technol. 6 (2015) 75–86.
[11] S. Simorgh, N. Alasvand, M. Khodadadi, F. Ghobadi, M. Malekzadeh Kebria, P. Brouki Milan, S. Kargozar, F. Baino, A. Mobasheri, M. Mozafari, Additive manufacturing of bioactive glass biomaterials, Methods 208 (2022) 75–91.

[12] F. Zhang, L. Zhu, Z. Li, S. Wang, J. Shi, W. Tang, N. Li, J. Yang, The recent development of vat photopolymerization: a review, Addit. Manuf. 48 (2021), 102423.
[13] X. Zhang, X. Jiang, C. Sun, Micro-stereolithography of polymeric and ceramic microstructures, Sens. Actuators, A 77 (1999) 149–156.
[14] I. Potestio, Lithoz: how lithography-based ceramic AM is expanding the opportunities for technical ceramics, Powder Inject. Mould. 13 (2019) 2–5.
[15] P. Tesavibul, R. Felzmann, S. Gruber, R. Liska, I. Thompson, A.R. Boccaccini, J. Stampfl, Processing of 45S5 Bioglass® by lithography-based additive manufacturing, Mater. Lett. 41 (2012) 81–84.
[16] S. Eqtesadi, A. Motealleh, P. Miranda, A. Pajares, A. Lemos, J.M.F. Ferreira, Robocasting of 45S5 bioactive glass scaffolds for bone tissue engineering, J. Eur. Ceram. Soc. 34 (2014) 107–111.
[17] E. Fiume, J. Massera, D. D'Ambrosio, E. Verné, F. Baino, Robocasting of multicomponent sol-gel–derived silicate bioactive glass scaffolds for bone tissue engineering, Ceram. Int. 48 (2022) 35209–35216.
[18] E. Fiume, S. Ciavattini, E. Verné, F. Baino, Foam replica method in the manufacturing of bioactive glass scaffolds: out-of-date technology or still underexploited potential? Materials 14 (2021) 2795.
[19] F. Baino, G. Magnaterra, E. Fiume, A. Schiavi, L.P. Tofan, M. Schwentenwein, E. Verné, Digital light processing stereolithography of hydroxyapatite scaffolds with bone-like architecture, permeability, and mechanical properties, J. Am. Ceram. Soc. 105 (2022) 1648–1657.
[20] A. Schiavi, E. Fiume, G. Orlygsson, M. Schwentenwein, E. Verné, F. Baino, High-reliability data processing and calculation of microstructural parameters in hydroxyapatite scaffolds produced by vat photopolymerization, J. Eur. Ceram. Soc. 42 (2022) 6206–6212.
[21] F. Baino, J. Barberi, E. Fiume, G. Orlygsson, J. Massera, E. Verné, Robocasting of bioactive SiO2-P2O5-CaO-MgO-Na2O-K2O glass scaffolds, J. Healthcare Eng. 2019 (2019), 5153136.
[22] E. Fiume, G. Serino, C. Bignardi, E. Verné, F. Baino, Sintering behavior of a six-oxide silicate bioactive glass for scaffold manufacturing, Appl. Sci. 10 (2020) 8279.
[23] A.D. Lantada, R.A. De Blas, M. Schwentenwein, C. Jellinek, J. Homa, Lithography-based ceramic manufacture (LCM) of auxetic structures: present capabilities and challenges, Smart Mater. Struct. 25 (2016), 054015.
[24] E. Fiume, D. Tulyaganov, G. Ubertalli, E. Verné, F. Baino, Dolomite-foamed bioactive silicate scaffolds for bone tissue repair, Materials 13 (2020) 628.
[25] ASTM C1239-07. Standard Practice for Reporting Uniaxial Strength Data and Estimating Weibull Distribution Parameters for Advanced Ceramics.
[26] T. Kokubo, H. Takadama, How useful is SBF in predicting in vivo bone bioactivity? Biomaterials 27 (2006) 2907–2915.
[27] A.L. Maçon, T.B. Kim, E.M. Valliant, K. Goetschius, R.K. Brow, D.E. Day, A. Hoppe, A.R. Boccaccini, I.Y. Kim, C. Ohtsuki, T. Kokubo, A. Osaka, M. Vallet-Regí, D. Arcos, L. Fraile, A.J. Salinas, A.V. Teixeira, Y. Vueva, R.M. Almeida, M. Miola, C. Vitale-Brovarone, E. Verné, W. Höland, J.R. Jones, A unified in vitro evaluation for apatite-forming ability of bioactive glasses and their variants, J. Mater. Sci. Mater. Med. 26 (2015) 115.
[28] T. Hildebrand, A. Laib, R. Müller, J. Dequeker, P. Rüegsegger, Direct three-dimensional morphometric analysis of human cancellous bone: microstructural data from spine, femour, iliac crest, and calcaneus, J. Bone Miner. Res. 14 (1999) 1167–1174.
[29] T.M. Link, V. Vieth, R. Langenberg, N. Meier, A. Lotter, D. Newitt, S. Majumdar, Structure analysis of high resolution magnetic resonance imaging of the proximal femur: in vitro correlation with biomechanical strength and BMD, Calcif. Tissue Int. 72 (2003) 156–165.
[30] V. Karageorgiou, D. Kaplan, Porosity of 3D biomaterial scaffolds and osteogenesis, Biomaterials 26 (2005) 5474–5491.
[31] F. Baino, M. Ferraris, O. Bretcanu, E. Verné, C. Vitale-Brovarone, Optimization of composition, structure and mechanical strength of bioactive 3-D glass-ceramic scaffolds for bone substitution, J. Biomater. Appl. 27 (2013) 872–890.
[32] Q.Z. Chen, I.D. Thompson, A.R. Boccaccini, 45S5 Bioglass®-derived glass–ceramic scaffolds for bone tissue engineering, Biomaterials 27 (2006) 2414–2425.
[33] O. Bretcanu, X. Chatzistavrou, K. Paraskevopoulos, R. Conradt, I. Thompson, A. R. Boccaccini, Sintering and crystallisation of 45S5 Bioglass® powder, J. Eur. Ceram. Soc. 29 (2009) 3299–3306.
[34] O. Peitl, G.P. LaTorre, L.L. Hench, Effect of crystallization on apatite layer formation of bioactive glass 45S5, J. Biomed. Mater. Res. 30 (1996) 509–514.
[35] L.L. Hench, Bioceramics: from concept to clinic, J. Am. Ceram. Soc. 74 (1991) 1487–1510.
[36] L.J. Gibson, Modelling the mechanical behavior of cellular materials, Mater. Sci. Eng. 110 (1989) 1–36.
[37] I.D. Thompson, L.L. Hench, Mechanical properties of bioactive glasses, glass-ceramics and composites, Proc. Inst. Mech. Eng. H 212 (1998) 127–137.
[38] J. Barberi, A. Nommeots-Nomm, E. Fiume, E. Verné, J. Massera, F. Baino, Mechanical characterization of pore-graded bioactive glass scaffolds produced by robocasting, Biomed. Glasses 5 (2019) 140–147.
[39] C. Vitale-Brovarone, G. Ciapetti, E. Leonardi, N. Baldini, O. Bretcanu, E. Verné, F. Baino, Resorbable glass-ceramic phosphate-based scaffolds for bone tissue engineering: synthesis, properties, and in vitro effects on humanmarrow stromal cells, J. Biomater. Appl. 26 (2011) 465–489.
[40] O. Bretcanu, F. Baino, E. Verné, C. Vitale-Brovarone, Novel resorbable glass-ceramic scaffolds for hard tissue engineering: from the parent phosphate glass to its bone-like microporous derivatives, J. Biomater. Appl. 28 (2014) 1287–1303.
[41] F.J. Martínez-Vázquez, F.H. Perera, P. Miranda, A. Pajares, F. Guiberteau, Improving the compressive strength of bioceramicrobocast scaffolds by polymer infiltration, Acta Biomater. 6 (2010) 4361–4368.
[42] S. Eqtesadi, A. Motealleh, A. Pajares, F. Guiberteau, P. Miranda, Improving mechanical properties of 13–93 bioactive glass robocast scaffold by poly(lactic acid) and poly(ε-caprolactone) melt infiltration, J. Non-Cryst. Solids 432 (2016) 111–119.
[43] Y. Shanjani, Y. Hu, R.M. Pilliar, E. Toyserkani, Mechanical characteristics of solid-freeform-fabricated porous calcium polyphosphate structures with oriented stacked layers, Acta Biomater. 7 (2011) 1788–1796.
[44] A.M. Galowa, A. Rebl, D. Koczan, S.M. Bonk, W. Baumann, J. Gims, Increased osteoblast viability at alkaline pH in vitro provides a new perspective on bone regeneration, Biochem. Biophys. Reports 10 (2017) 17–25.
[45] L.L. Hench, Bioactive ceramics, Ann. N. Y. Acad. Sci. 523 (1988) 54–71.
[46] A. López-Noriega, D. Arcos, I. Izquierdo-Barba, Y. Sakamoto, O. Terasaki, M. Vallet-Regi, Ordered mesoporous bioactive glasses for bone tissue regeneration, Chem. Mater. 18 (2006) 3137–3144.
[47] C. Renghini, V. Komlev, F. Fiori, E. Verné, F. Baino, C. Vitale-Brovarone, Micro-CT studies on 3-D bioactive glass-ceramic scaffolds for bone regeneration, Acta Biomater. 5 (2009) 1328–1337.